Optical tissue clearing enables rapid, precise and comprehensive assessment of three-dimensional morphology in experimental nerve regeneration research

Simeon C. Daeschler[1, *], Jennifer Zhang[1, 3], Tessa Gordon[1, 3], Gregory H. Borschel[1, 2, 3, 4]

From the Contents

Graphical Abstract *Three-dimensional histomorphology of intact, optically cleared peripheral nerve and target organs*
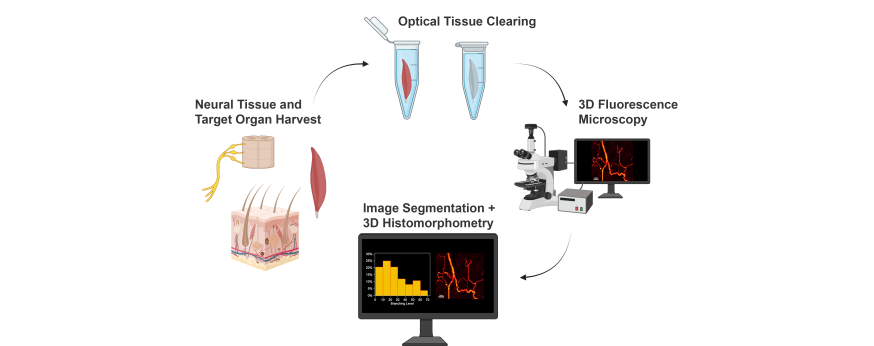
Abstract

Morphological analyses are key outcome assessments for nerve regeneration studies but are historically limited to tissue sections. Novel optical tissue clearing techniques enabling three-dimensional imaging of entire organs at a subcellular resolution have revolutionized morphological studies of the brain. To extend their applicability to experimental nerve repair studies we adapted these techniques to nerves and their motor and sensory targets in rats. The solvent-based protocols rendered harvested peripheral nerves and their target organs transparent within 24 hours while preserving tissue architecture and fluorescence. The optical clearing was compatible with conventional laboratory techniques, including retrograde labeling studies, and computational image segmentation, providing fast and precise cell quantitation. Further, optically cleared organs enabled three-dimensional morphometry at an unprecedented scale including dermatome-wide innervation studies, tracing of intramuscular nerve branches or mapping of neurovascular networks. Given their wide-ranging applicability, rapid processing times, and low costs, tissue clearing techniques are likely to be a key technology for next-generation nerve repair studies. All procedures were approved by the Hospital for Sick Children's Laboratory Animal Services Committee (49871/9) on November 9, 2019.

Key Words: histology; image segmentation; morphometry; nerve regeneration; outcome assessment; peripheral nerve; three-dimensional imaging; tissue clearing

Chinese Library Classification No. R446; R361; Q2

Introduction

Experimental nerve regeneration studies often rely on microscopic morphological analysis of nerve tissue and target organs to assess experimental outcomes. Traditionally, morphological analysis requires tissue sectioning to enable microscopic examination because light scattering limits the sampling depth to a few micrometers. Although tissue sectioning has been successfully used throughout decades of biomedical research, it disrupts the three-dimensional tissue architecture and bears the risk of cutting artifacts. Moreover, large organs such as the spinal cord or skeletal muscle in adult rat models often generate hundreds of serial tissue sections. Consequently, quantitative morphological analysis usually requires sampling of selected sections or regions of interest and subsequent extrapolation. Extrapolation inherently introduces bias to quantitative outcome metrics. Particularly in the analysis of sparsely and non-uniformly distributed structures, such as neuromuscular junctions in skeletal muscle, relevant information in other sections may be missed, and morphometrics may lose precision and accuracy. Robust techniques that enable the detailed analysis of entire intact organs thus may improve the reliability of morphometrics

[1]SickKids Research Institute, Neuroscience and Mental Health Program, Toronto, ON, Canada; [2]Institute of Biomaterials and Biomedical Engineering, University of Toronto, Toronto, ON, Canada; [3]Division of Plastic and Reconstructive Surgery, the Hospital for Sick Children, Toronto, ON, Canada; [4]Indiana University School of Medicine, Indianapolis, IN, USA

***Correspondence to:** Simeon C. Daeschler, MD, simeondaeschler@gmail.com.

https://orcid.org/0000-0001-8130-7714 (Simeon C. Daeschler)

and at the same time provide morphological data on an unprecedented scale.

Recent advancements in laboratory tissue processing techniques now enable researchers to render entire organs completely transparent in a chemical process termed optical tissue clearing (Richardson and Lichtman, 2015). In conjunction with the expression of fluorescent proteins in transgenic animal models or post-mortem immunostaining, target structures in cleared organs can be visualized in a preserved three-dimensional tissue architecture (Erturk et al., 2011; Hama et al., 2011; Renier et al., 2014; Neckel et al., 2016; Belle et al., 2017). The tissue clearing process first harmonizes the refractive index of the processed specimen by removing lipids, pigments and water and then matches the refractive index with an imaging solution to minimize light scattering (Erturk et al., 2011; Richardson and Lichtman, 2015). The achieved tissue transparency enables the almost unrestricted penetration of light and thus allows for fluorophore excitation even in deep tissue layers that were previously inaccessible in intact tissue (Richardson and Lichtman, 2015).

Over the last decade optical tissue clearing techniques have largely transformed neuroscience of the brain by enabling brain-wide studies of the rodent connectome (Hama et al., 2011; Ertürk and Bradke, 2013; Neckel et al., 2016; Qi et al., 2019; Ueda et al., 2020), Yet their application in experimental nerve regeneration research is presently rare. Here we describe how we adapted and applied previously developed, solvent-based optical tissue clearing techniques to enable comprehensive morphological assessments in whole organs relevant to nerve repair studies.

Materials and Methods

This study is reported in accordance with the ARRIVE 2.0 guidelines (Animal Research: Reporting of *In Vivo* Experiments)(Percie du Sert et al., 2020). All procedures were performed in strict accordance with the National Institutes of Health guidelines, the Canadian Council on Animal Care (CCAC) and were approved by the Hospital for Sick Children's Laboratory Animal Services Committee (49871/9; approval date: November 9, 2019).

Experimental animals

We included six adult (10–12 weeks old, 250–300 g), female transgenic rats with a Sprague-Dawley genetic background (Moore et al., 2012). This in-house bred transgenic strain endogenously expresses green fluorescent protein (GFP) in motor and sensory neurons under the Thy-1 promotor (Thy-1 GFP[+]) and therefore allows label-free nerve fiber detection via fluorescence microscopy (Magill et al., 2010; Moore et al., 2012). All animals were housed in a central animal care facility with fresh water and pellet food ad libitum. A constant room temperature (22°C) and a circadian rhythm of 12 hours per 24 hours illumination were automatically maintained.

Retrograde neuronal labeling *in vivo*

All surgical procedures were performed under aseptic conditions and inhalational anesthesia with an Isoflurane (Baxter, IL, USA) oxygen mixture (3%, flow: 2 L/min). For analgesia, 4 mg/kg body weight extended-release Meloxicam (Metacam, Boehringer Ingelheim, Ingelheim, Germany) was injected subcutaneously. The rat was placed on a heating pad to maintain body temperature and the left hind leg was shaved and surgically cleaned with an alcohol/betadine rub. The common peroneal nerve was exposed within anatomical planes through a dorsolateral-gluteal muscle-splitting incision and cut 5 mm distal to the sciatic bifurcation. The wound bed including the adjacent peripheral nerves were carefully covered with a sterile, fluid-repellent drape to prevent leakage of the fluorescent tracer. The end of the proximal common

peroneal nerve segment was placed in a well containing 5 μL of 4% Fluoro-Gold (Fluorochrome LLC, Denver, CO, USA) in double-distilled water. Sterile petroleum jelly was used to keep the nerve in place and prevent desiccation. After 60 minutes, the wounds were thoroughly irrigated with saline, dried, and closed in three layers with 5-0 Vicryl (Ethicon, Raritan, NJ, USA) sutures. Experimental animals were recovered in a warm environment prior to returning to the housing facility.

Tissue harvest and fixation

Seven days after the retrograde labeling procedure, the rats were euthanized and the entire spinal cord and the dorsal root ganglia (DRG) from L1 to L6 were harvested bilaterally using a hydraulic extrusion technique as previously described (Richner et al., 2017). This method allows for rapid tissue harvest with a low risk of inadvertent tissue damage and thereby overcomes the need for transcardial perfusion. We further harvested the contralateral common peroneal nerve and peroneus longus muscle and a full-thickness skin flap of the contralateral dorsal hind-paw. The specimens were fixed by immersion in pre-cooled 4% paraformaldehyde (PFA) at 4°C for 24 hours, then washed and stored in precooled PBS in the dark at 4°C until further processing. Detailed laboratory protocols are included in the supplemental material. For the skin flaps, we applied light compression in a petri dish for the 1st hour of fixation to flatten the sample. Similarly, flattening by compression can be used for large skeletal muscles when the imaging objective has a limited working distance.

Immunostaining

For heavily colored specimens, such as muscle or skin, we added a decolorization step in 25% Quadrol (Cat# 122262, Sigma-Aldrich, St. Louis, MO, USA) in double-distilled water at 37°C for 2 days with daily changes of the solution prior to the immunostainings. The following antibodies were used: rabbit anti-beta 3 tubulin (neural cell marker; Cat# ab18207, 1:200 dilution, Abcam, Cambridge, UK; incubation at 37°C for 2–4 days) with goat anti-rabbit Alexa Fluor 555 conjugated secondary antibody (Cat# A-21428, RRID:AB_141784, 1:300 dilution, Invitrogen, Waltham, MA, USA; incubation at 37°C for 2–3 days).

For tail vein injections 1 hour prior to euthanasia we used 20 μg α-bungarotoxin conjugated with Alexa Fluor 647 (Cat# B35450, Thermo Fisher Scientific, Waltham, MA, USA) to stain the neuromuscular junctions (NMJ) or 30 μg Alexa Fluor 647 conjugated CD31 antibody (Cat# 102516, Biolegend, San Diego, CA, USA) to label the vasculature in 200 μL sterile saline respectively (Chen et al., 2016).

We used whole-organ immunostainings as previously described (Qi et al., 2019). Briefly, after fixation and optional decolorization, the samples were pretreated in ascending methanol series (50%, 80%, 2 × 100% methanol in double-distilled H_2O for 30 minutes each) followed by an overnight step in 5% H_2O_2/20% dimethyl sulfoxide (DMSO, 276855, Sigma-Aldrich)/methanol at 4°C to reduce background fluorescence and increase permeability. Subsequently, the samples were treated in 100% methanol for 45 minutes twice followed by two 45-minute steps in 20% DMSO/methanol and a descending methanol series (80%, 50% methanol in double-distilled H_2O for 30 minutes each). Then the samples were washed in PBS for 1 hour twice followed by an overnight step. Next samples were permeabilized in PBS/0.2% Triton X-100 (Sigma-Aldrich)/20% DMSO/0.3 M glycine overnight at 37°C and blocked in PBS/0.2% Triton X-100/10% DMSO/5% normal donkey serum for 3 days. Following two 2-hour washing steps in PTwH (PBS/0.2% Tween-20 (P9416, Sigma-Aldrich)/0.01 mg/mL Heparin) the sample was immersed in primary antibody dilutions in PTwH/5% DMSO/3% normal donkey serum at 37°C for 2–4 days, followed by a 2-day wash in PTwH on a shaker with four changes of the washing solution. Then the samples

were incubated in secondary antibody diluted in PTwH/3% normal donkey serum for 2–4 days at 37°C followed by a 2-day wash in PTwH on a shaker with at least four changes of the washing solution.

Optical tissue clearing

For optical tissue clearing, we used a modified FDISCO protocol (Qi et al., 2019). Prior to an optical clearing, we embedded the DRGs in PBS/1% Agarose gel columns in one plane to facilitate subsequent image acquisition. For optical clearing, the tissue was immersed in an ascending series of precooled (4°C) tetrahydrofuran (Cat# 186562, Sigma-Aldrich) double distilled water solutions (50%, 75%, 3 × 100%) for dehydration and delipidation. Triethylamine (Cat# 471283, Sigma-Aldrich) was used to adjust the pH of the solutions to 9.0 and all steps were performed in the dark at 4°C on an orbital shaker (Qi et al., 2019). For further delipidation of a particularly lipid-rich specimen such as the spinal cord, we used a subsequent step in 100% dichloromethane (Cat# 270997, Sigma-Aldrich) at room temperature. The immersion time ranged between 30 minutes and 2 hours for each step, depending on the tissue type and specimen size (**Additional file 1**). We do not recommend prolonged solvent incubation to minimize quenching. Then the specimen was immersed in ethanol/dibenzyl ether (Cat# 108014, Sigma-Aldrich) solutions overnight at 4°C in the dark, with two changes of the solution, to match the refractive index of the tissue with the microscope objective. To optimize the imaging solution for glycerol/CLARITY (clear lipid-exchanged acrylamide-hybridized rigid imaging/immunostaining/in situ-hybridization-compatible tissue-hydrogel) objectives, we determined the best trade-off between transparency-dependent imaging depth and spherical aberration in ascending ethanol/dibenzyl ether solutions for each tissue. The process is visualized in **Figure 1**.

Imaging, data processing and analysis

Although we recommend imaging within 3 days following tissue clearing, in our experience selected fluorophores (e.g., fluorogold) allow for storage for up to 6 months at 4°C in the dark without significant quenching. For image acquisition of cleared spinal cord and DRGs we used a 3D light-sheet fluorescence microscope (Zeiss Lightsheet Z.1, Carl Zeiss Microscopy GmbH, Jena, Germany) equipped with a p.co edge 5.5 Camera (PCO AG, Kehlheim, Germany) and a CLARITY objective (20× magnification, 1.0 numerical aperture) optimized for a refractive index of 1.45. For Fluoro-Gold labeled specimen we used a 405 nm (20 mW) laser and Zeiss Zen Lightsheet 2014 software (Carl Zeiss Microscopy GmbH). To enable automated batch processing and comparative analysis, we used consistent illumination plane settings and laser intensities of 2.5%.

Damage to the objective was prevented by exposure to dibenzyl ether, we used borosilicate glass tubing (Kavalierglass A.S., Křížová, Czech Republic) to separate the immersed specimen from the microscope optics. This tubing matches the refractive index of the adjusted tissue (1.472) and is resistant to the dibenzyl ether (Carro et al., 2015). For cleared peripheral nerves, skeletal muscle, and skin flaps we used a Leica SP8 LIGHTNING confocal microscope (DMI8, Leica Microsystems, Wetzlar, Germany), equipped with Leica LAS software, a Hybrid detector (HyD), and a p.co Edge 5.5 camera (PCO AG, Kelheim, Germany). We used a 20×/0.75 (W) and a 40×/1.3 (W) objective with the following lasers: 405 nm (50 mW), 488 nm (20 mW), 552 nm (20 mW), 638 nm (30 mW). For inverted confocal microscopy, we used Cell Imaging Dishes with a 1.0 µm thin cover glass bottom (Eppendorf AG, Hamburg, Germany) to leverage the full working distance of the objective for maximum imaging depth.

For data processing, we used arivis Vision 4D (version 3.0,

arivis AG, Rostock, Germany) or Leica LAS (Leica Microsystems, Wetzlar, Germany) for three-dimensional tile stitching, Huygens deconvolution software (Scientific Volume Imaging, Hilversum, Netherlands), and Imaris (Version 9.5.1, Bitplane AG, Zurich, Switzerland) for image segmentation, fluorescence measurements, and quantitative morphometric analyses. Selected images in this publication are created with BioRender.com.

Conventional tissue processing and manual quantification of retrogradely-labeled neurons

To validate the software-based neuron counting in the optically cleared spinal cord and DRGs we compared the results against the conventional enumeration technique in serial cryosections. Therefore, we performed Fluoro-Gold retrograde labeling on three randomly selected rats and harvested the tissue with the above-mentioned techniques. The specimens were fixed in 4% PFA at 4°C for 48 hours and then in 4% PFA with 30% sucrose for cryoprotection for 2–5 days at 4°C. The Spinal cord and DRGs (L1 to L6) were then embedded in Tissue Freezing Medium (Electron Microscopy Sciences, Hatfield, USA) and frozen at –80°C for a minimum of 12 hours. Then the tissue blocks were mounted in a cryostat microtome (CM3050S, Leica Microsystems, Wetzlar, Germany) and cut in 50 µm longitudinal sections (spinal cord) or 20 µm transverse sections (DRG) as previously described (Zuo et al., 2020). The tissue sections were mounted on Superfrost Plus microscope glass slides (Fisher Scientific, Pittsburgh, PA, USA) and examined under an epifluorescence microscope (Leica DM2500, Leica Microsystems) at 10× magnification. A blinded examiner counted the Fluoro-Gold-labeled neurons in every spinal cord section and every fifth DRG section (Zuo et al., 2020). The total motoneuron counts were calculated with the widely used Abercrombie correction factor to account for double counted, split neuronal cell bodies that partially lie in two adjacent sections (Abercrombie, 1946).

Statistical analysis

For statistical analysis, we used JMP (version 15.1.0, SAS Institute, Cary, NC, USA). Descriptive statistics were calculated, and means are expressed with standard deviations (SD). To compare the cell counts based on image segmentation in cleared tissue and the estimations in tissue sections, we used tissue of healthy rats because the variability induced by nerve injury and repair, would have increased variability and thereby the necessary sample size. We considered a difference of 50 motoneurons to be worth reporting and assumed an SD of 15 based on preliminary experiments, requiring a sample size of $n = 3$ per group to achieve a power of 0.8 on a significance level of 5% (normally distributed, two-tailed t-test). To test for normality of continuous variables, we used normal quantile plots and Anderson-Darling tests. For pairwise comparison of normally distributed, continuous data we used two-tailed Student's t-tests. For non-normally-distributed variables we used Wilcoxon tests. To determine the predictive ability of fluorescence intensity thresholds to discriminate neuron populations, we used receiver operating characteristic (ROC) analyses. A significance level of 5% was used ($P < 0.05$).

Results

Refractive index matching

Specialized microscopes are available with optics optimized for the high refractive index (1.56) of cleared tissue immersed in pure dibenzyl ether. However, widely used glycerol or CLARITY objectives are optimized with a refractive index of around 1.45. The refractive index mismatch between sample and objective creates blurred images due to spherical aberration (Richardson and Lichtman, 2015). To overcome the refractive index mismatch for those objectives, we used immersion in ethanol/dibenzyl ether solutions as previously described (Carro et al., 2015). Lowering the refractive index of the immersion

solution, however, inevitably affects sample transparency. To optimize the imaging solution for glycerol/CLARITY objectives, we determined the best trade-off between transparency-dependent imaging depth and spherical aberration due to refractive index mismatch in ascending ethanol/dibenzyl ether solutions. The best images were achieved with a 34.1% (v/v) ethanol in dibenzyl ether solution for spinal cords, and a 30.1 vol% solution for agarose embedded DRGs.

Retrograde labeling studies in the intact spinal cord and dorsal root ganglia

Investigators rely heavily on the quantification of regenerated motor and sensory neurons following experimental nerve repair to evaluate the extent of nerve regeneration. However, conventional tissue sectioning is labor intensive, susceptible to cutting artifacts, and requires correction factors to estimate the true number of neurons (Abercrombie, 1946). To overcome these challenges, we used a modified FDICSO protocol to clear intact spinal cord and entire dorsal root ganglia (DRGs) of adult rats and to quantify fluorescently labeled neurons via automated image segmentation (**Figure 1**).

Using immersion in a series of commercially available solvents, we achieved almost complete transparency for both, spinal cord and DRGs within 24 hours (**Figures 2** and **3**). Thereafter, the immersed specimens were imaged via fluorescence microscopy. We found light-sheet microscopy to be best suited to large, cleared tissue specimens, due to the rapid image acquisition, minimal photobleaching, and high spatial resolution (**Figure 2A–C**).

As compared to manual cell counts in tissue sections, three-dimensional imaging of the entire spinal cord and intact DRGs allows for precise quantitation of all labeled neurons. However, manual annotation of labeled cells in large tissue volumes is time-consuming. To streamline the quantitative analysis of the terabyte-sized data sets, we determined the applicability of automated image segmentation based on cell body dimensions and fluorescence intensity thresholds (**Figure 2D–F** and **I–L**). First, we manually tagged retrogradely labeled and unlabeled (autofluorescent) neurons in the spinal cord and DRGs (L1 to L6) of three adult rats that had previously undergone retrograde labeling of the left common peroneal nerve with the fluorescent tracer Fluoro-Gold. We measured the average voxel fluorescence intensity per cell body of the Fluoro-Gold labeled neurons (n = 1792 motoneurons; n = 3421 sensory neurons) and randomly selected unlabeled, autofluorescent neurons (n = 1120 motoneurons; n = 1774 sensory neurons, **Figure 2G** and **M**). The fluorescence intensity of the labeled motoneurons was significantly higher compared to the autofluorescence intensity of unlabeled motoneurons (673.5 ± 109.3 *vs*. 385.3 ± 37.5, *P* < 0.001). Similarly, the Fluoro-Gold labeled sensory neurons in cleared DRGs had a significantly higher fluorescence intensity than the unlabeled cell bodies (1774.8.2 ± 506.5 *vs*. 533.3 ± 52.9, *P* < 0.001). We then used ROC analyses to determine the diagnostic performance of automated segmentation of labeled neurons amongst different experimental animals based on a consistent fluorescence intensity threshold. We used the manual segmentations as a standard and identified a mean fluorescence intensity per cell of 481.4 to be the optimal cut-off value for discriminating Fluoro-Gold labeled motoneurons from autofluorescent neurons (sensitivity: 99.3%; specificity of 98.7%; ROC area under the curve 0.9996, **Figure 2H**). For sensory neurons we found even higher discriminatory accuracy using an intensity threshold of 872.1 (sensitivity: 100%; specificity of 100%; ROC area under the curve 1.0, **Figure 2P**), indicating complete differentiation between the labeled neurons versus the unlabeled (autofluorescent) cell populations. The higher fluorescence intensities of DRG neurons are most likely a result of the smaller tissue volume compared to spinal cords and thus less light scattering during

fluorophore excitation and emission.

We then compared the neuron counts in the optically cleared spinal cord and DRGs against the estimates derived from conventional cell counting technique in serial tissue sections in age-matched control rats (*n* = 3). Without correction for split cells, the number of labeled motoneurons that were counted in tissue sections significantly exceeded the neuron number in the optically cleared spinal cord (697 ± 16 *vs*. 569 ± 23, *P* = 0.001). Similarly, the mean number of sensory neurons counted in sections of DRG L1 to L6 was substantially higher compared to the counts in cleared DRG's (6138 ± 345 *vs*. 2632 ± 94, *P* < 0.001). To correct for double counted, split cells in tissue sections, we applied the Abercrombie correction factor (Abercrombie, 1946). We calculated a correction factor of 0.56 for motoneuron counts and 0.36 for sensory neuron counts based on median cell body diameters of 38.5 μm for motoneurons (*n* = 375 measured cell bodies) and 34.9 μm for sensory neurons (*n* = 400 measured cell bodies). Compared to the corrected cell counts, we identified 46% more labeled motor (*P* < 0.001) and 19% more sensory neurons (*P* = 0.009) in optically cleared, intact tissue, indicating a significant overcorrection by the Abercrombie factor (**Figure 3B** and **C**). We further noted an approximate 50% reduction of tissue processing time in the tissue clearing group compared to the conventional technique previously used in our laboratory (**Figure 3A**). Those time savings were primarily attributed to the superfluous cryoprotection and labor-intensive steps such as embedding, cryosectioning, and manual cell counting as part of the conventional protocol.

Three-dimensional image segmentation of cleared organs enables a wide range of quantitative assessments of fluorescently labeled cell populations beyond automated enumeration. Possible measurements include, but are not limited to, volumetric or dimensional measurements of single cells or entire cell populations, as demonstrated in **Figure 2N** and **O**. Here we measured the cell body volume (median 26 885.8 μm^3) and the maximum cell diameter (median 53.2 μm) of retrogradely labeled sensory neurons that project their axons in the common peroneal nerve. As shown in the histograms of **Figure 2N** and **O**, multiple local maxima can be distinguished indicating the inclusion of morphologically distinct cellular subpopulations. Application of previously established population thresholds may allow for detailed differentiation of those subpopulations in optically cleared neural ganglia.

Mapping the neurovascular network in optically cleared peripheral nerves

Sufficient blood supply is essential to clear debris and establish a pro-regenerative environment following peripheral nerve injury. Accordingly, ischemia has been described as a determining pathomechanism in neuropathies and a key length-limiting factor for acellular nerve allografts and synthetic conduits (Best et al., 1999; Ostergaard et al., 2015; Goncalves et al., 2017). However, the historically challenging assessment of the neurovascular network in three dimensions has been a limiting factor for conclusive morphological studies. We used optical tissue clearing techniques to render peripheral nerve segments transparent and thereby make the intraneural vascular network accessible for high-resolution fluorescence microscopy (**Figure 4A**). In specimens harvested from animals that did not undergo transcardial perfusion, vessels still contained red blood cells which are intensely autofluorescent in the green emission spectrum. This can already be used as a broad approximation to map larger blood vessels, but in smaller capillaries, we found the distribution of red blood cells to be inconsistent. We therefore used an intravenous injection of fluorescently conjugated CD31 antibody to label the endothelial walls of the entire vascular network. Using a far-red emission spectrum, we

obtained consistent staining across upper and lower extremity peripheral nerves. Automated blood vessel tracing based on fluorescence intensity thresholds enabled mapping of the neurovascular network including capillaries with an inner diameter below that of red blood cells (< 6 μm) as shown in **Figure 4B–D**. Beyond visualization and qualitative assessment, we were able to segment the blood vessels in inter-branch segments for detailed quantitative analysis. Exemplary, we segmented a 1000 μm segment of a rat common peroneal nerve (**Figure 4**). The inner diameter of the intraneural blood vessels ranged between 4.0 μm and 23.5 μm, averaging 11.6 ± 3.3 μm (**Figure 4D**). Most inter-branch segments were short (< 40 μm), but some blood vessels spanned over almost 400 μm between two branch points (**Figure 4E**). When analyzing the angle between the vascular axis and the longitudinal nerve axis, the blood vessels were predominantly longitudinally oriented, as previously described (Best and Mackinnon, 1994). However, approximately 5% of the inter-branch segments were orientated perpendicular to the nerve axis, representing perforators that connect epi- and perineural to endoneurial blood vessels (**Figure 4F**).

Tracing neural projections in target organs

Transparent skeletal muscles allow for comprehensive analysis of intramuscular neuronal projections and their neuromuscular junctions. This may be used to quantitatively assess the re-innervation process following peripheral nerve repair or determine disease-related changes in the neuromuscular architecture. We used threshold-based filament tracing to visualize motor nerve branches within a peroneus longus muscle of a Thy-1 GFP+ rat, a commonly used target muscle for experimental nerve repair studies (**Figure 4G** and **H**). Notably, PFA fixed skeletal muscle features a pronounced autofluorescence in the green and red emission spectrum (**Figure 4H**), making far-red the preferred fluorophore for muscle imaging due to a higher signal-to-noise ratio, as previously described (Williams et al., 2019). To visualize the NMJs, we intravenously injected α-Bungarotoxin conjugated with a fluorescent marker in the far red-spectrum (Chen et al., 2016). Similar to principles of transcardial perfusion, tail vein injections use the blood flow to distribute the conjugated antibody evenly throughout the entire system. Thereby, the injections rapidly achieve homogenous stainings of intact muscles that are otherwise difficult for antibodies to penetrate with post-mortem immunohistochemistry (Chen et al., 2016). Homogenous NMJ stainings can be confirmed after tissue clearing. NMJ morphology is remarkably stable in rodents with intact nerves (Balice-Gordon and Lichtman, 1990). In response to denervation or reinnervation, however, NMJs undergo substantial structural reorganization and change their appearance and surface area (Rich and Lichtman, 1989). Such metrics can be precisely quantified on a large scale in optically cleared skeletal muscle. To demonstrate their applicability, we randomly segmented a region of interest measuring $0.5 \times 0.5 \times 1.0$ mm^3 within a rat peroneus longus muscle within which we identified a total of $n = 52$ separate neuromuscular junctions. Using the Imaris surface tool, we created surfaces with 0.3 μm surface detail for each NMJ to quantify the three-dimensional surface area (**Figure 4I** and **J**). The surface area of the physiologically innervated NMJ's ranged from 2840.3 μm^2 to 9712 μm^2 with an average area of 5167.2 ± 1475.3 μm^2 (**Figure 4K**).

Dermatome-wide cutaneous innervation studies in cleared skin

To determine the applicability of optical clearing techniques to assess skin innervation, we harvested full-thickness skin flaps from the sural nerve dermatome of adult Sprague Dawley rats. Immediately before harvest, we applied hair removal cream (Veet, Reckitt Benckiser, UK) to remove the strongly autofluorescent hairs. To facilitate imaging, we flattened the skin flaps with gentle pressure during the first hour of PFA fixation. Subsequently, the samples were decolorized, permeabilized, and immunostained against neuronal cell markers. Given the green autofluorescence and rapid, solvent-induced quenching of endogenous GFP expressed under the Thy-1 promoter in this rat model, we used additional immunostaining against beta-3-tubulin to improve signal-to-noise ratio. Using optical tissue clearing, the full-thickness skin flaps were rendered transparent and then imaged via confocal microscopy. Despite moderate autofluorescence in the red spectrum, the cutaneous nerve branches were clearly visible (**Figure 5A** and **B**). Within each nerve branch, individual axons were distinguishable that terminated in free- or lanceolate nerve endings in the skin and around hair follicles (**Figure 5E**). To quantitatively assess the cutaneous innervation, we segmented a region of interest of 2500 μm × 2000 μm (**Figure 5B–D**). The skin innervation density, defined as nerve branch length per region of interest area, was 9508.9 μm/mm^2. Of note, this is 2.6-fold lower compared to the nerve fiber density in the cornea of the same rat strain (Catapano et al., 2018). The median branching angle of the cutaneous nerve fibers was 33.9° and the median branch length was 63.85 μm. We found 56 free nerve endings per mm^2, some of which arose from nerve branches with more than 60 branching points within the region of interest, demonstrating the arborized architecture of the cutaneous nerve plexus (**Figure 5F**).

Discussion

Here we demonstrate the applicability of optical tissue clearing to experimental nerve regeneration studies. Optical tissue clearing methods have been introduced to overcome imaging depth limitations in harvested tissue by reducing light scattering to a level of almost complete transparency (Erturk et al., 2011; Richardson and Lichtman, 2015). In conjunction with light-sheet fluorescence microscopy and powerful data processing tools, these techniques enable organ-wide morphological readouts and objective analysis with subcellular resolution. This has revolutionized the field of brain connectomics (Schneider-Mizell et al., 2016) and holds similar promise for morphological studies of the peripheral nervous systems in development, health, and disease.

A variety of tissue clearing techniques have been developed and continuously refined, each having its respective advantages and drawbacks for different research applications (Ertürk and Bradke, 2013; Renier et al., 2014; Neckel et al., 2016; Jing et al., 2018; Qi et al., 2019). In our laboratory, we adopted a slightly modified FDISCO protocol due to its powerful clearing capabilities, rapid processing times, low costs, and easy applicability requiring only conventional laboratory equipment. We were able to process entire organs with this solvent-based technique and thereby overcame the risk of cutting artifacts in precious experimental samples. The protocols have been proven to reliably provide high levels of transparency for all tested organs. When the level of transparency was insufficient due to application errors or following long-term storage, immersion in 100% tetrahydrofuran can simply be repeated even months after the initial clearing process to readjust the refractive index and achieve excellent transparency.

Adopting optical tissue clearing techniques in our laboratory has increased time efficiency by overcoming labor-intensive steps such as cryosectioning and manual cell counting. This method also avoids time-consuming transcardial perfusion with PFA and instead uses hydraulic extrusion of the spinal cord (Richner et al., 2017). Beyond substantially increased time efficiency, this method does not require dissections of PFA-soaked animals and thus drastically decreases the associated risk of accidentally damaging the spinal cord and avoids exposure to hazardous fumes.
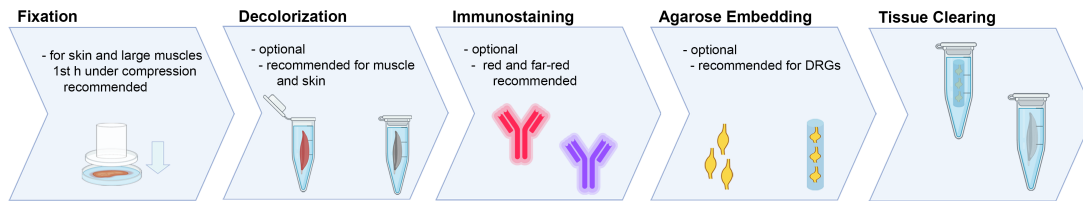
Figure 1 | Tissue processing steps for optical clearing.
After fixation by immersion in paraformaldehyde, an optional decolorization step for tissues that include high amounts of pigments (such as hemo- and myoglobin) is followed by whole organ immunostainings, preferably with red or far-red fluorophores. To streamline the image acquisition process, small organs can be embedded in agarose gel and imaged together. Thereafter, the samples undergo optical clearing in pH 9.0 adjusted and precooled (4°C) solvents in the dark. Then the cleared samples can be imaged or stored in the imaging solution, depending on the fluorophore stability. DRG: Dorsal root ganglia.
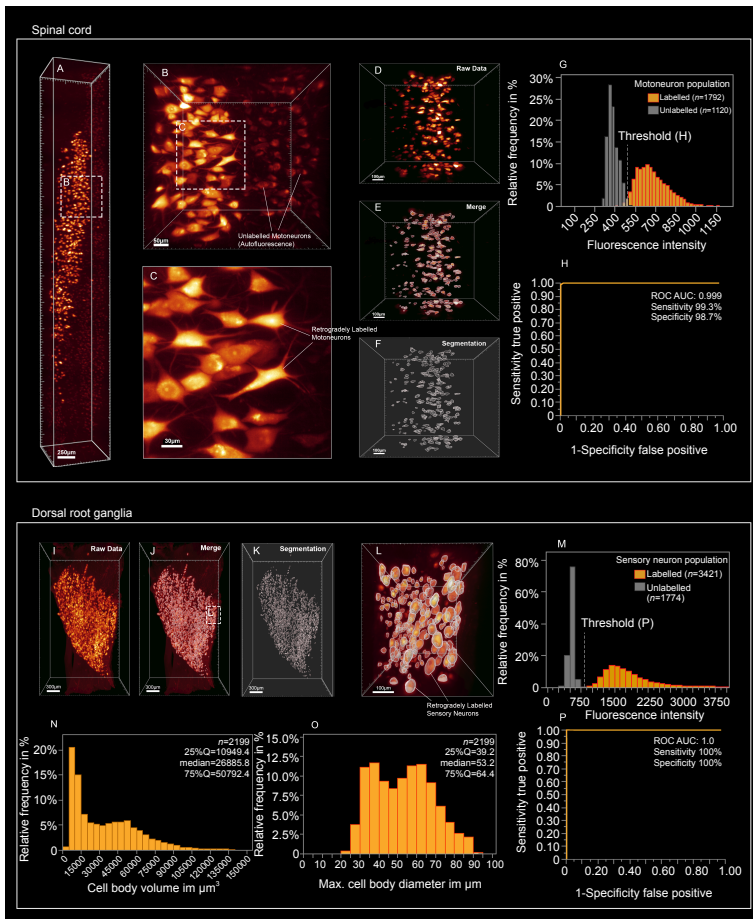
Figure 2 | Neuron segmentations in the optically cleared spinal cord and dorsal root ganglia.
(A) Retrogradely labeled motoneurons in the ventral horn that project their axons in the common peroneal nerve. (B) Higher magnification of labeled and autofluorescent cell bodies (scale bar). (C) Labeled motoneuron cell bodies in higher magnification (scale bar). (D) Raw fluorescence microscopy image of labeled motoneurons. (E) Automated motoneuron segmentations as overlay/merge with the raw data image in D. (F) Automated motoneuron segmentations of the image in D only. (G) The significantly different mean voxel fluorescence intensity per cell of labeled and autofluorescent neurons enables precise, automated discrimination of labeled and unlabeled motoneurons via fluorescence intensity thresholds (ROC curve in H). (I) Optically cleared L4 dorsal root ganglion after retrograde labeling of the common peroneal nerve. A segmentation of the same DRG is shown in J and K and in higher magnification in L. (M) Similar to motoneurons, labeled sensory neurons can be identified based on fluorescence intensity with high precision and accuracy. Such automated segmentation of fluorescently labeled sensory neurons provide population-wide metrics including cell body volume in (N) and maximum cell body diameter in (O) showing two histogram maxima that may indicate labeling of at least two morphologically distinct neuronal subpopulations. Scale bars: 250 μm in A, 50 μm in B, 30 μm in C, 100 μm in D–F. AUC: Area under the curve; Q: quartile; ROC: receiver operating analysis.
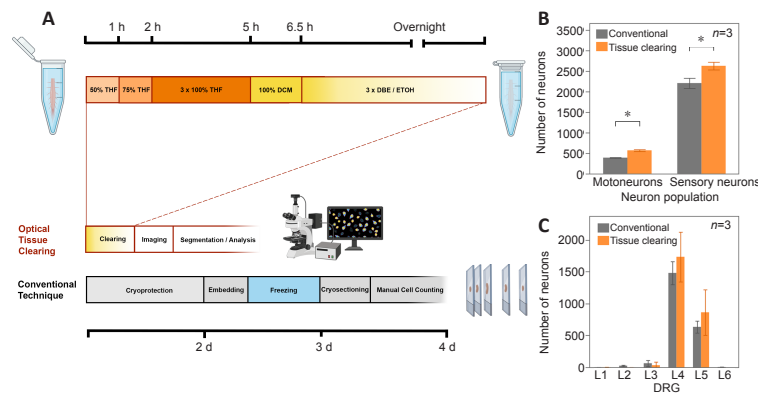

Figure 3 | Comparing optical tissue clearing and the conventional cryosection technique for the quantitative assessment of retrogradely labeled common peroneal nerve neurons.
(A) Processing steps for fixed tissue in both techniques, indicating substantial time savings when tissue clearing is used compared to cryosections. (B) Comparing the number of motor and sensory neurons derived from optically cleared (orange) and cryosectioned tissue (grey), showing that significantly more neurons were identified in intact, cleared spinal cord and DRGs. (C) The number of labeled common peroneal nerve sensory neurons that have been identified by both techniques in the dorsal root ganglia from L1 to L6. The results indicate a tendency of the conventional technique to overestimate cell counts in ganglia with few labeled neurons (L2 and L3) and to underestimate neuron counts in ganglia with a high density of labeled cells (L4 and L5), although the differences did not reach statistical significance in this experiment ($P > 0.05$). DBE: Dibenzyl ether; DCM: dichloromethane; DRG: dorsal root ganglia; ETOH: ethanol; THF: tetrahydrofuran.
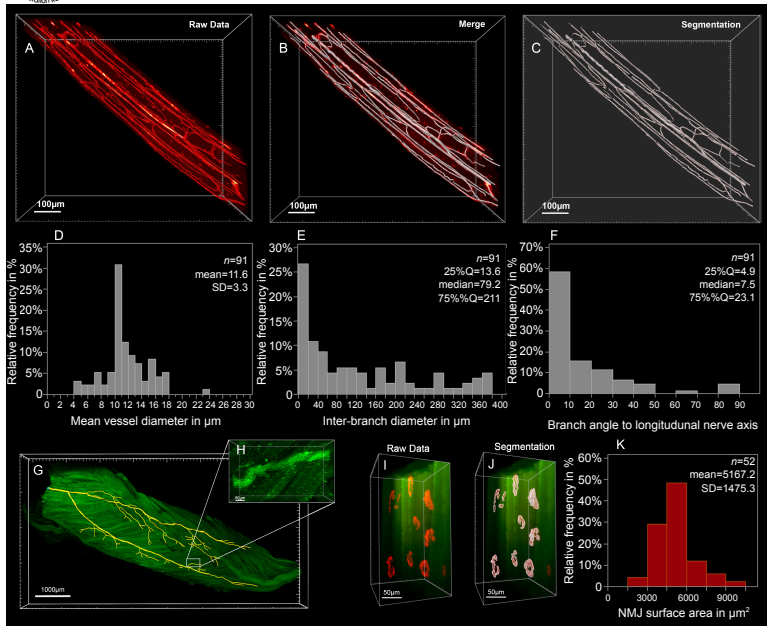
Figure 4 | Filament tracing in optically cleared peripheral nerve and skeletal muscle.
(A) Fluorescently labeled neurovascular system in a rat common peroneal nerve segment. Segmentations as seen in B and C can compartmentalize the blood vessel network in inter-branch segments and thereby allow for detailed analysis of the blood vessel diameter (D), the distance between two branching sites (E) or the angle of the vascular axis (F). (G) Similar fluorescence-based filament tracing techniques can be used to map the intermuscular nerve branches in the peroneus longus muscle of a transgenic Thy-1 GFP⁺ rat with green-fluorescent axons (scale bar). (H) Intramuscular nerve branch in higher magnification (scale bar) (I) Neuromuscular junctions stained with fluorescently conjugated α-bungarotoxin (red) can be mapped via image segmentation (white overlay in J) in cleared muscle and quantitatively analyzed for their three-dimensional surface area (K) to determine structural changes related to development or disease. Of note, GFP-positive axon terminal innervating the NMJs are not visible with the applied imaging parameters. Scale bars: 100 µm in A–C, I, and J, 1000 µm in C, 50 µm in H. NMJ: Neuromuscular junction; Q: quartile; SD; standard deviation.
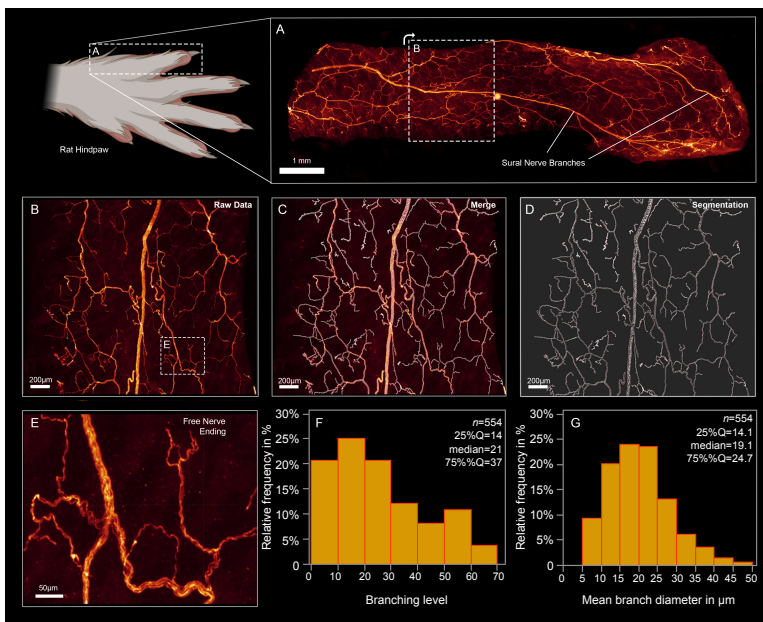

Figure 5 | Cutaneous innervation in the rat sural nerve dermatome.
(A) A full-thickness skin graft from the dorsum of the fifth toe was harvested, immunostained against the neuronal marker beta-3-tubulin (red) and optically cleared for fluorescence imaging. (B) Cutaneous nerve branches in higher magnification. (C) Segmentation of the cutaneous innervation as an overlay/merge with the raw image shown in B. (D) Nerve fiber segmentation only. (E) Cutaneous nerve branches with free nerve endings in high magnification. The histogram in (F) displays the percentage frequency of the branching levels of the cutaneous nerve plexus, after compartmentalization into inter-branch segments. The branching level describes the number of branch points proximal to a segment. (G) The percentage frequency of the average diameter of a nerve branch. Scale bars: 1 mm in A, 200 µm in B, 200 µm in C, D, 50 µm in E. Q: Quartile.

For retrograde labeling studies in this experiment, the inconsistent, multisegmental distribution of sensory neurons that project their axons into a peripheral nerve necessitates the examination of multiple DRGs per experimental animal to reliably capture all neurons. When using conventional tissue sectioning techniques, each DRG represents hours of work. Investigators consequently limit the number of examined specimens to one or two ganglia per animal (e.g. L4 and L5 for common peroneal nerve studies) (Tajdaran et al., 2019; Zuo et al., 2020). Due to their time- and work efficiency, tissue clearing techniques overcome these limitations in this study. To further streamline the imagine acquisition process, we embedded all relevant DRGs of the same animal together in 1% agarose gel columns before tissue clearing. Thereby we were able to reduce the number of required microscope setups and further increase time efficiency.

Three-dimensional imaging with high spatial resolution in all planes allows for reliable application of automated segmentations and subsequent quantitative analysis based on objective parameters. This is in stark contrast to manual cell counting in serial tissue sections where, among cells with high fluorescence intensity, a subset of weakly stained cells often present investigators with challenges whether to count the cell or not. Such numerical insecurities are further amplified by double-counted split cells and the consequent need to apply correction factors to estimate the true number of cells (Abercrombie, 1946). This study observed that neuron counts derived from conventional tissue sections exceed the true number of retrogradely labeled neurons but the Abercrombie correction factor tends to overcorrect neuron counts. This study also shows that automated cell counting, based on a predefined intensity threshold provides highly accurate cell counts, with a sensitivity above 99.3% and specificity greater 98.7%. The ROC analyses further indicated the excellent performance of a consistent threshold for discriminating Fluoro-Gold labeled cells from autofluorescent cells across different experimental animals. This substantially reduces observer-introduced bias for retrograde neuronal labeling experiments and was possible by standardizing the labeling (dye concentration and exposure time), tissue processing (fixation and immersion times), and imaging procedures (laser intensity, resolution, z-step-size). We prefer Fluoro-Gold for

retrograde labeling experiments due to its high signal-to-noise ratio. However, for laboratories without access to confocal or light-sheet microscopes with compatible UV excitation lasers, we recommend alternative tracers, such as Fluororuby.

Comprehensive analysis of the re-organization of neural projections following nerve surgery, particularly nerve transfers, is critical to better understand their functional impact in rodent models and translate experimental results in well-founded clinical hypotheses. An advantage of optically cleared tissue is the preserved three-dimensional tissue architecture. Tracing filamentous structures with a high length-to-diameter ratio, such as nerve fibers, that span across in large tissue volumes has been historically challenging in tissue sections (Helmstaedter et al., 2011). The high tissue transparency achieved by optical clearing now provides the opportunity to map the entire neuromuscular connectome of a regenerating nerve and thereby unveils an unprecedented level of information for morphological outcome assessments in experimental nerve repair studies. Particularly for the study of complex arborized networks, such as axons or blood vessels, three-dimensionality inherently provides a better understanding of spatial relations and structural coherences. Of note, we have demonstrated the capabilities of software-assisted segmentation and quantitative assessment for the neurovascular network in a rat common peroneal nerve. By compartmentalizing the vascular network in inter-branch segments, we were able to differentiate distinct vessel types by diameter and projection angle to quantitatively analyze the intraneural blood vessel architecture in great detail. Such morphometrics may be valuable to study the reorganization of the vascular network in long allografts or assess neurovascular pathologies.

Optical tissue clearing, in conjunction with light-sheet fluorescence microscopy, enables rapid data acquisition for large, intact tissue volumes. This allows for large-scale morphometric analysis without sacrificing subcellular resolution. For nerve repair studies, these capabilities can be leveraged for neuromuscular junction morphometry in a skeletal muscle or dermatome-wide cutaneous innervation studies. Although conventional two-dimensional analysis of arborized neural projections, such as assessing intra-epidermal nerve fiber density in skin biopsies, has been proven to be valuable in determining disease progression of systemic neuropathies, such approaches do not accurately reflect the complex neural morphology. This holds particularly true when nerve fibers are unequally distributed across the region of interest, such as during the process of skin reinnervation following nerve repair. We demonstrated that clearing techniques may be used to render large, full-thickness skin samples transparent, enabling rapid, objective and detailed morphometric readouts of entire dermatomes and thus providing unprecedented insights into the cellular activities governing cutaneous (re-)innervation. Consequently, readily applicable clearing protocols may inspire attention to the reorganization of the sensory system in future nerve repair studies, in both skin as well as any other tissue type.

While adopting optical tissue clearing and computational image segmentations for our research, we faced several challenges. First, endogenous fluorophores may be susceptible to quenching during solvent exposure depending on the animal model. We recommend minimizing the solvent exposure time and using only fresh, pre-cooled, and pH-adjusted solvents. Post-mortem immunostaining may further improve fluorescence intensity for selected antigens. However, for post-mortem immunostaining of dense, intact organs such as skeletal muscle, antibody penetration may be limited which can result in inconsistent staining in the center of the sample. Novel permeabilization protocols such as FLASH (Messal et al., 2021) may improve antibody penetration in large intact samples post-mortem. Alternatively, selected antigens can

be stained reliably with *in vivo* antibody injections into the tail vein that, thereby, may render the time-consuming and unreliable post-mortem immunostaining superfluous. Further, imaging whole organs instead of selected tissue sections may require hours of confocal microscopy time per sample, depending on the resolution. This may hinder the adoption of this technique for large-scale experiments in laboratories with restricted access to microscopes. Modern light-sheet microscopes, however, allow the imaging time to be reduced greatly and therefore, are recommended for optically cleared tissue.

Imaging intact organs, however, comes with the inherent limitation of a restricted number of target structures that can be visualized in the same sample. This is due to the limited number of distinguishable fluorescent emission spectra during image acquisition. To overcome this limitation, other, hydrogel-based techniques have been developed that allow for multiple rounds of de- and re-stainings of the same specimen (Murray et al., 2015). Another limitation that must be considered is the dehydration-associated effect of tissue shrinkage that occurs in solvent-based tissue clearing protocols. This must be considered when interpreting morphometry. Conversely, tissue shrinkage facilitates the deep imaging of large samples that otherwise would exceed the maximum working distance of high–numerical aperture objectives.

Since 2011, the field of optical tissue clearing and whole-organ immunostaining is rapidly evolving (Erturk et al., 2011). Novel machine learning models are already on the horizon and are going to streamline the further segmentation process of large, multiple terabyte-sized image stacks by reducing manual processing steps and potential observer bias. Presently developed panoptic imaging methods and compatible microscopes are soon going to enable rapid imaging of entire, optically cleared rodents (Cai et al., 2019). In conjunction with capable machine learning models and transgenic animal models (e.g. brainbow mice), this will allow for automated tracing of the entire neural connectome of the central and peripheral nervous system in the same experimental animal, likely offering exciting insights in biological processes and a deeper understanding of systemic reorganization after nerve injury and repair.

Conclusion

We demonstrated the applicability of optical tissue clearing techniques and computational image segmentation for a variety of tissues relevant to experimental nerve repair studies and outlined their potential benefits and current limitations. Integrating those techniques into our research has increased time efficiency while enabling objective and accurate morphological studies on an unprecedented scale. Given the advantages of optical tissue clearing over conventional methods, this technique is likely to be a key technology for future experimental studies of nerve injury and repair.

References

Abercrombie M (1946) Estimation of nuclear population from microtome sections. Anat Rec 94:239-247.

Balice-Gordon RJ, Lichtman JW (1990) In vivo visualization of the growth of pre- and postsynaptic elements of neuromuscular junctions in the mouse. J Neurosci 10:894-908.

Belle M, Godefroy D, Couly G, Malone SA, Collier F, Giacobini P, Chédotal A (2017) Tridimensional visualization and analysis of early human development. Cell 169:161-173.e112.

Best TJ, Mackinnon SE (1994) Peripheral nerve revascularization: a current literature review. J Reconstr Microsurg 10:193-204.

Best TJ, Mackinnon SE, Midha R, Hunter DA, Evans PJ (1999) Revascularization of peripheral nerve autografts and allografts. Plast Reconstr Surg 104:152-160.

Cai R, Pan C, Ghasemigharagoz A, Todorov MI, Förstera B, Zhao S, Bhatia HS, Parra-Damas A, Mrowka L, Theodorou D, Rempfler M, Xavier ALR, Kress BT, Benakis C, Steinke H, Liebscher S, Bechmann I, Liesz A, Menze B, Kerschensteiner M, et al. (2019) Panoptic imaging of transparent mice reveals whole-body neuronal projections and skull-meninges connections. Nat Neurosci 22:317-327.

Carro M, Paroutis P, Woolside M, Harrison R (2015) Improved Imaging of Cleared Samples with ZEISS Lightsheet Z.1:Refractive Index on Demand. In. Zeiss.com: Carl Zeiss Jena.

Catapano J, Antonyshyn K, Zhang JJ, Gordon T, Borschel GH (2018) Corneal neurotization improves ocular surface health in a novel rat model of neurotrophic keratopathy and corneal neurotization. Invest Ophthalmol Vis Sci 59:4345-4354.

Chen W, Yu T, Chen B, Qi Y, Zhang P, Zhu D, Yin X, Jiang B (2016) In vivo injection of α-bungarotoxin to improve the efficiency of motor endplate labeling. Brain Behav 6:e00468.

Erturk A, Mauch CP, Hellal F, Forstner F, Keck T, Becker K, Jahrling N, Steffens H, Richter M, Hubener M, Kramer E, Kirchhoff F, Dodt HU, Bradke F (2011) Three-dimensional imaging of the unsectioned adult spinal cord to assess axon regeneration and glial responses after injury. Nat Med 18:166-171.

Ertürk A, Bradke F (2013) High-resolution imaging of entire organs by 3-dimensional imaging of solvent cleared organs (3DISCO). Exp Neurol 242:57-64.

Goncalves NP, Vaegter CB, Andersen H, Ostergaard L, Calcutt NA, Jensen TS (2017) Schwann cell interactions with axons and microvessels in diabetic neuropathy. Nat Rev Neurol 13:135-147.

Hama H, Kurokawa H, Kawano H, Ando R, Shimogori T, Noda H, Fukami K, Sakaue-Sawano A, Miyawaki A (2011) Scale: a chemical approach for fluorescence imaging and reconstruction of transparent mouse brain. Nat Neurosci 14:1481-1488.

Helmstaedter M, Briggman KL, Denk W (2011) High-accuracy neurite reconstruction for high-throughput neuroanatomy. Nat Neurosci 14:1081-1088.

Jing D, Zhang S, Luo W, Gao X, Men Y, Ma C, Liu X, Yi Y, Bugde A, Zhou BO, Zhao Z, Yuan Q, Feng JQ, Gao L, Ge WP, Zhao H (2018) Tissue clearing of both hard and soft tissue organs with the PEGASOS method. Cell Res 28:803-818.

Magill CK, Moore AM, Borschel GH, Mackinnon SE (2010) A new model for facial nerve research: the novel transgenic Thy1-GFP rat. Arch Facial Plast Surg 12:315-320.

Messal HA, Almagro J, Zaw Thin M, Tedeschi A, Ciccarelli A, Blackie L, Anderson KI, Miguel-Aliaga I, van Rheenen J, Behrens A (2021) Antigen retrieval and clearing for whole-organ immunofluorescence by FLASH. Nat Protoc 16:239-262.

Moore AM, Borschel GH, Santosa KB, Flagg ER, Tong AY, Kasukurthi R, Newton P, Yan Y, Hunter DA, Johnson PJ, Mackinnon SE (2012) A transgenic rat expressing green fluorescent protein (GFP) in peripheral nerves provides a new hindlimb model for the study of nerve injury and regeneration. J Neurosci Methods 204:19-27.

Murray E, Cho JH, Goodwin D, Ku T, Swaney J, Kim S-Y, Choi H, Park YG, Park JY, Hubbert A, McCue M, Vassallo S, Bakh N, Frosch MP, Wedeen VJ, Seung HS, Chung K (2015) Simple, scalable proteomic imaging for high-dimensional profiling of intact systems. Cell 163:1500-1514.

Neckel PH, Mattheus U, Hirt B, Just L, Mack AF (2016) Large-scale tissue clearing (PACT): Technical evaluation and new perspectives in immunofluorescence, histology, and ultrastructure. Sci Rep 6:34331.

Ostergaard L, Finnerup NB, Terkelsen AJ, Olesen RA, Drasbek KR, Knudsen L, Jespersen SN, Frystyk J, Charles M, Thomsen RW, Christiansen JS, Beck-Nielsen H, Jensen TS, Andersen H (2015) The effects of capillary dysfunction on oxygen and glucose extraction in diabetic neuropathy. Diabetologia 58:666-677.

Percie du Sert N, Ahluwalia A, Alam S, Avey MT, Baker M, Browne WJ, Clark A, Cuthill IC, Dirnagl U, Emerson M, Garner P, Holgate ST, Howells DW, Hurst V, Karp NA, Lazic SE, Lidster K, MacCallum CJ, Macleod M, Pearl EJ, et al. (2020) Reporting animal research: Explanation and elaboration for the ARRIVE guidelines 2.0. PLoS Biol 18:e3000411.

Qi Y, Yu T, Xu J, Wan P, Ma Y, Zhu J, Li Y, Gong H, Luo Q, Zhu D (2019) FDISCO: Advanced solvent-based clearing method for imaging whole organs. Sci Adv 5:eaau8355.

Renier N, Wu Z, Simon DJ, Yang J, Ariel P, Tessier-Lavigne M (2014) iDISCO: a simple, rapid method to immunolabel large tissue samples for volume imaging. Cell 159:896-910.

Rich MM, Lichtman JW (1989) In vivo visualization of pre- and postsynaptic changes during synapse elimination in reinnervated mouse muscle. J Neurosci 9:1781-1805.

Richardson DS, Lichtman JW (2015) Clarifying tissue clearing. Cell 162:246-257.

Richner M, Jager SB, Siupka P, Vaegter CB (2017) Hydraulic Extrusion of the Spinal Cord and Isolation of Dorsal Root Ganglia in Rodents. J Vis Exp:55226.

Schneider-Mizell CM, Gerhard S, Longair M, Kazimiers T, Li F, Zwart MF, Champion A, Midgley FM, Fetter RD, Saalfeld S, Cardona A (2016) Quantitative neuroanatomy for connectomics in Drosophila. Elife 5:e12059.

Tajdaran K, Chan K, Shoichet MS, Gordon T, Borschel GH (2019) Local delivery of FK506 to injured peripheral nerve enhances axon regeneration after surgical nerve repair in rats. Acta Biomater 96:211-221.

Ueda HR, Ertürk A, Chung K, Gradinaru V, Chédotal A, Tomancak P, Keller PJ (2020) Tissue clearing and its applications in neuroscience. Nat Rev Neurosci 21:61-79.

Williams MPI, Rigon M, Straka T, Hörner SJ, Thiel M, Gretz N, Hafner M, Reischl M, Rudolf R (2019) A novel optical tissue clearing protocol for mouse skeletal muscle to visualize endplates in their tissue context. Front Cell Neurosci 13:49.

Zuo KJ, Shafa G, Antonyshyn K, Chan K, Gordon T, Borschel GH (2020) A single session of brief electrical stimulation enhances axon regeneration through nerve autografts. Exp Neurol 323:113074.